

Key Points:

- The precise range and magnitude of gas discharges in the southern Okinawa Trough are determined by processing the SBES data
- The magnitude and intensity of gas discharges can be attributed to volcanic fluid activity or structural faults
- The three-dimensional flares observed in the water column illustrate the impact of tides on the upward movement of gas plumes

Correspondence to:

J.-Y. Lin,
jylin@ncu.edu.tw

Citation:

Lin, Y. C., Lin, J.-Y., Hsu, S.-K., Chen, S.-C., Lin, S.-S., & Tsai, C.-H. (2024). Gas emission characteristics and tectonic implications in the southernmost Okinawa Trough from split-beam echo sounder observations. *Journal of Geophysical Research: Oceans*, 129, e2023JC020176. <https://doi.org/10.1029/2023JC020176>

Received 3 JULY 2023

Accepted 5 FEB 2024

Author Contributions:

Conceptualization: Jing-Yi Lin, Shu-Kun Hsu, Ching-Hui Tsai

Data curation: Shiao-Shan Lin, Ching-Hui Tsai

Formal analysis: Yi Chin Lin

Funding acquisition: Song-Chuen Chen

Investigation: Jing-Yi Lin

Methodology: Yi Chin Lin, Jing-Yi Lin

Project administration: Shiao-Shan Lin

Resources: Shu-Kun Hsu, Song-Chuen Chen, Shiao-Shan Lin

Software: Yi Chin Lin

Supervision: Shu-Kun Hsu, Shiao-Shan Lin






Validation: Yi Chin Lin

Visualization: Yi Chin Lin, Jing-Yi Lin

Writing – original draft: Yi Chin Lin

Writing – review & editing: Jing-Yi Lin

Gas Emission Characteristics and Tectonic Implications in the Southernmost Okinawa Trough From Split-Beam Echo Sounder Observations

Yi Chin Lin¹ , Jing-Yi Lin¹ , Shu-Kun Hsu¹ , Song-Chuen Chen² , Shiao-Shan Lin³, and Ching-Hui Tsai³ 

¹Department of Earth Sciences, National Central University, Taoyuan City, Taiwan, ²Central Geological Survey, Ministry of Economic Affairs, New Taipei City, Taiwan, ³Center for Environmental Studies, National Central University, Taoyuan, Taiwan

Abstract Traditionally, single-beam echo sounder (SBES) data are used to determine the position of emission structures in the form of a two-dimensional profile, which may not be straightforward enough to correlate the data of adjacent profiles and determine the exact discharge area. In this study, we develop semiautomatic software to remove noise and select possible flare signals to enhance the speed and precision of the data processing. The program also allows for the transformation of the data into a three-dimensional point cloud distribution by computing the receiving angle of the data. By applying this method to investigate the distribution and mechanism of gas emission structures in the South Okinawa Trough (SOT), we determine four high flux areas and 22 isolated plumes with roots. Widespread gas flares usually occur in areas with large-scale volcanic activity or gas-enriched structures. Isolated gas plumes could be found for a single knoll outcrop and normal faulting structures. The energy of the flares around the knoll area is generally stronger than that observed along the normal faults. Compared with other geophysical data, we find that the widespread distribution of gas flares generally implies a larger hydrothermal potential, which may not be revealed by single-profile acoustic image observations. We also find that the direction of flares is strongly influenced by tides, and the height of the flare represents the thermocline as a strong boundary for bubbles composed by carbon dioxide.

Plain Language Summary This study introduces a new method using SBES data to analyze gas emission structures in the South Okinawa Trough. By developing specialized software, the researchers enhance the speed and precision of data processing, allowing for the identification of high flux areas and isolated plumes. The study reveals that widespread gas flares indicate significant hydrothermal potential, influenced by tides and thermocline height. This research expands our understanding of gas emissions in the region.

1. Introduction

Occupying the eastern margin of the Eurasian continent, the Okinawa Trough (OT) extends from southwest Kyushu Island to the Ilan Plain of Taiwan (Figure 1). Characterized by an active normal faulting system in its upper crust and numerous volcanic outcrops, the OT shows a typical morphology of a back-arc basin, which is suggested to be in the rifting stage (Kimura et al., 1988; Lee et al., 1980; Letouzey & Kimura, 1986; Sibuet et al., 1987, 1998; Uyeda, 1987). This tectonic setting is usually prone to relatively high heat flow, making the OT a potential site for hydrothermal exploration. The presence of microbial communities and hydrothermal minerals in the middle and northern OT also confirms this possibility (Glasby & Notsu, 2003; Halbach et al., 1989; Ishibashi, Ikegami, et al., 2014; Ishibashi, Noguchi, et al., 2014; Kimura et al., 1988; Luders & Niedermann, 2010; Minami & Ohara, 2017; Sakai et al., 1990; Toki et al., 2016; Uyeda, 1987). The Southern Okinawa Trough (SOT) has a more pronounced back-arc basin structure with a relatively deeper water depth and larger width than the middle and northern OT (Figure 1). However, few hydrothermal-related studies have been conducted due to the lack of appropriate instruments and systematic observations. In 2016, a 4-year program entitled “Geological Investigation of Mineral Resource Potential in the Offshore Area of Northeastern Taiwan”, including geological, geophysical, geochemical, and seafloor observations, was launched under the support of the Central Geological Survey (CGS), Ministry of Economic Affairs (MOEA) in Taiwan. Not only did the data obtained from different aspects provide information about the tectonic context of the SOT, but the integration of observations in diverse domains also improved our knowledge about the hydrothermal environment in a similar tectonic context (Chen et al., 2019).

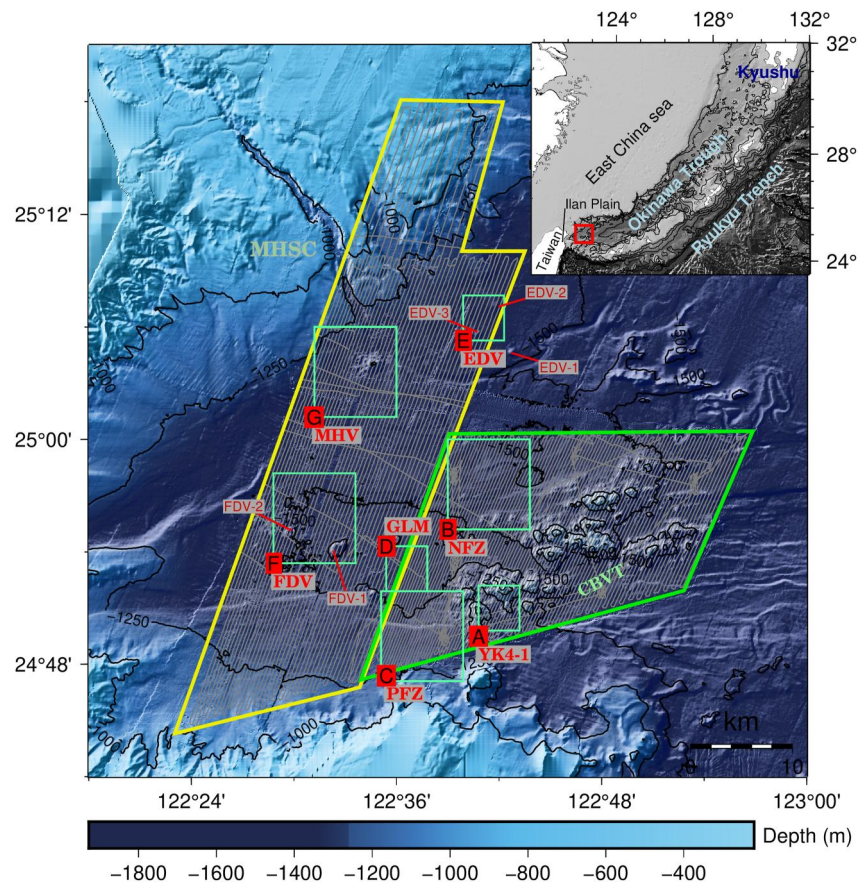


Figure 1. Bathymetry and potential hydrothermal site (thin green rectangle) distribution in the Southern Okinawa Trough. Gray lines in thick green and yellow contours show the survey tracks of the echo sounder experiment in 2016 and 2017, respectively. OT: Okinawa Trough; YK4-1: Yonaguni Knoll IV; NFZ: Normal Fault Zone; PFZ: Penglai Fault Zone; GLM: Geolin Mounds; EDV: Earth Dragon Volcano; FDV: Fire Dragon Volcano; MHV: Meinhun Volcano; MHSC: Mein-Hua Submarine Canyon; CBVT: Cross Back-arc Volcanic Trail.

The acquisition of data from oceanographic explorations and expeditions is always a crucial element for ocean science studies. In the 1970s, bathymetric and seismic reflection investigations were the most commonly used geophysical survey methods for understanding the marine environment and petroleum exploration. During the past two decades, with improvements in marine instrumental technologies, studies on different research aspects in marine sciences have become possible. Studies with innovative and more specific proposals have been initiated to meet the urgent needs of climate change evaluation and new energy discoveries, such as the rise of seawater temperature leading to the dissociation of shallow gas hydrates. Westbrook et al. (2009), the time variation of methane emissions behavior (Jerram et al., 2015) and the quantification of the emissions scale (Römer et al., 2012; Schneider von Deimling et al., 2011). However, the introduction of new instruments is generally costly. The limitation of implementing these high-tech instruments may impede the progress of our knowledge of this ocean and reduce our ability to address current environmental and energy-related issues. Therefore, how to extract a new value or any additional information from the data acquired from previous experiments with relatively less sophisticated instruments could also be of great importance. Single-beam echo sounding (SBES) is one of the most basic data collected for marine geophysics research. By emitting pulses and recording reflection signals, echo-sounding systems provide information about the seawater and seabed. However, due to the relatively low coverage and precision, its data are rarely used currently for most marine geophysical research. Our study aims to develop a new echo sounder data processing procedure, hereafter named EK due to the common system used for the data collection. The objective is to establish software that systematically processes widespread EK data. In addition, instead of along-track displayed 2-dimensional EK images, we extract the 3-dimensional EK structures for the gas plumes, allowing a better investigation of the degassing mechanisms and processes. We then apply this

method to study the hydrothermal environment of the SOT. The comparison between the 3-dimensional features of the gas plumes and other available geological data in the SOT allows us to decrypt the possible relationships between the gas plume patterns and their geological destinations. Whenever the correlation is established, a similar procedure could be applied to other areas where the use of advanced instruments is still unlikely to increase our background knowledge of the area.

2. Geological Background

The Okinawa Trough is the back-arc basin of the Ryukyu subduction system, where the Philippine Sea Plate is subducting beneath the Eurasian Plate. The sequence of back-arc basin development in the southwestern part of the OT has been crustal thinning, with the smallest crustal thickness of approximately 15 km in the central graben area (Klingelhoefer et al., 2009). Geophysical and bathymetric data indicate numerous normal faults, which usually cut through sedimentary layers and extend to the seafloor. Such an active normal faulting system belongs to the most recent extensional phase in the Pleistocene–Holocene (0.1–0 Ma) in the N170° direction (Kimura, 1985; Miki, 1995; Sibuet et al., 1998). In addition, another normal faulting system is also defined in the N150° direction, which is the product of the previous extensional phase that occurred in the Pleistocene (2–0.1 Ma). Volcanic knolls are distinct on the seafloor (Miki, 1995; Park et al., 1998; Shinjo et al., 1999). The most obvious example is the Cross Back-arc Volcanic Trail (CBVT), which consists of a group of approximately 70 submarine volcanoes (Figure 1) (Chung et al., 2000; J.-Y. Lin et al., 2004; Sibuet et al., 1998). Located near the southern end of the CBVT volcanic area, Yonaguni Knoll IV-1 (YK4-1) (Figure 1) is the first studied hydrothermal site in the SOT. Numerous oceanographic experiments have provided obvious evidence for its intense hydrothermal activity, such as the existence of massive sulfide deposits, sulfide chimneys, active black smokers, and extremely high heat flow (Gena et al., 2013; Inagaki et al., 2006; Ishibashi, Ikegami, et al., 2014; Ishibashi, Noguchi, et al., 2014; Nunoura et al., 2010; Suzuki et al., 2008). Except for the CBVT area, several volcanic outcrops were also reported in the center of the central axis of the SOT. The most obvious should be Fire Dragon Volcano 1 (FDV-1) and Fire Dragon Volcano 2 (FDV-2). This group of volcanism is usually located in the central depression of the SOT (area F in Figure 1). The volcanoes without outcrops on the seafloor are defined as the Earth Dragon volcanic group, which comprises Earth Dragon Volcano 1 (EDV-1), Earth Dragon Volcano 2 (EDV-2), and Earth Dragon Volcano 3 (EDV-3) (area E in Figure 1). Instead of being located near the central axis, we observed this type of volcano near the northern border of the SOT to the southeast of the Mein-Hua Submarine Canyon (MHSC). The Mein-Hua Volcano (MHV) area (area G in Figure 1), located at the foot of the MHSC, is an outlier. Even though it is situated far from the central graben of the SOT, we still observed clear volcanic morphology. More recently, two potential hydrothermal sites without volcano-like shapes have also been revealed in the SOT from deep-towed side-scan sonar images and subbottom profile data: the Penglai Fault zone (PFZ) and the Geolin Mounds (GLM) (areas C and D in Figure 1) (Chen et al., 2019; Hsu, 2017). An apparent acoustically transparent zone was imaged in the shallow sediments of the two sites (Hsu, 2017), suggesting a very active fluid/gas circulation system (Hsu, 2017; Hsu et al., 2019). In addition, the low magnetic anomalous behavior of the two sites also suggests a high hydrothermal potential due to hydrothermal alteration and metasomatism (Doo et al., 2019; Huang et al., 2019).

3. Materials and Methods

Several oceanographic experiments, supported by the CGS in Taiwan, have been performed in the SOT to explore the submarine mineral potential during the past 4 years. The EK data from the April 2016 and April 2017 experiments, containing 132 survey lines with a total length of 4,585.1 km, are used in this study (gray lines in Figure 1). The equipment employed for the data requisition is the Simard TM EK60 split-beam echo sounder (38 and 120 kHz) system onboard the R/V Ocean Research 2. For the parameters set, the beam width of the transducer is 7.6° along with the ship and 6.4° athwart ship. A pulse duration of 4 ms and a sample interval of 1.024 ms are applied for the source, and the source energy level is set to 2,000 W. The ping interval is 3 s, and the average ship speed is 5–6 knots, resulting in an approximately 9.2 m-long distance between two pings. The survey line interval is approximately 300 m in the 2016 experiment and 350 m in 2017. Since the water depth of the survey area ranges between 800 and 1,600 m, the theoretical footprint in the study area also varies between 94 and 188 m. In addition, we only processed the sound signals acquired from the 38 kHz source, focusing on a relatively low-frequency band, to decrease the attenuation of sound energy in water.

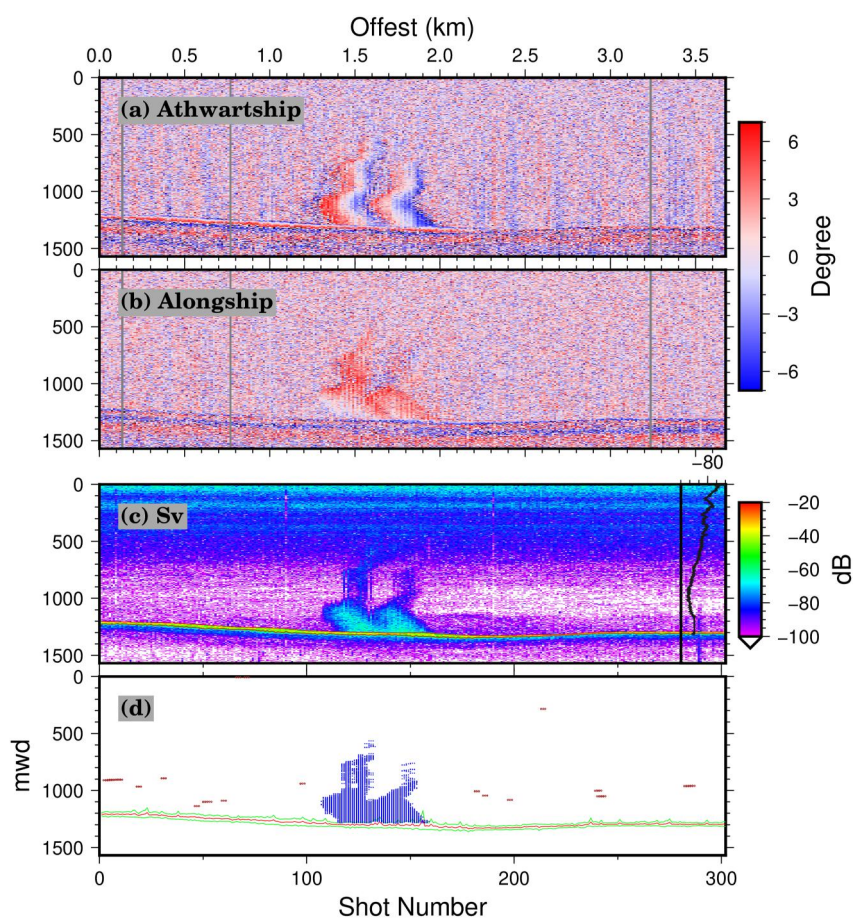


Figure 2. Example of the parameters used in the data processing procedure for the single-beam echo sounder system (SBES) of the water column. (a) and (b) show the athwart ship and the along-ship mechanical angle. Positive numbers denote the fore and starboard directions. (c) Denotes one example of the volume backscattering strength (Sv) distribution along one water column profile. Flare signals show higher energy when the water depth is larger than 1,000 m. The black line in its left-hand side figure shows the average background noise level. (d) The distribution of flare signals after data processing performed by our software. Brown and blue dots represent the random and detected signals, respectively. The lower energy located in the upper part of the flares could still be well detected. Green lines indicate the upper and lower envelopes of the sea floor backscatter energy. The red line shows the seabed detection of the maximum value.

Generally, EK data are analyzed by the 2-D image-displayed method, which shows the energy intensity of the reflected sound waves along survey lines. In this way, the dimension of target objects may not be correctly estimated because of the uncertainty of several factors, such as the ship speed, the sample interval, the beam resolution, and the angle between the ship direction and the flare. To obtain EK data with higher accuracy and precision, we first developed Fortran-based software that allows the systematic processing of EK data with higher efficiency. A 3-D visualization is also generated to provide a better method for target area illustration. This software also integrated mechanical angle information from along ship and athwart ship directions, which we can extract from the EK data log (e.g., Figures 2a and 2b), to calculate the depth and offset for each bin per ping. In addition to the attenuation correction, the volume backscattering strength (Sv, dB re 1 m^{-1}), which indicates the sum of the energy of a unit volume (Clay & Medwin, 1977; Jerram et al., 2015), is also calculated to reveal a more accurate pattern for the signal density distribution (Figure 2c). The heading recorded by the GPS stream can be used for a better estimation of Sv. However, the signal strength cannot be wholly calibrated due to the lack of the full hull attitude in the header. Even though this situation may affect the coordinates of the transmitted and received signals for several to dozens of meters, the error is relatively minor and can be included in the error caused by the sampling interval. Due to the near-vertical incidence angle of the SBES, errors induced by the water velocity profiles are predominantly manifested in the vertical direction. Taking extreme velocities of 1,480 m/s and 1,520 m/s at a slant range of 1,300 m as an example, the one-way travel time difference amounts to 23 ms. At

an incidence angle of 3°, the disparity in the horizontal direction is less than 2 m, significantly below the resolution threshold. Therefore, the influence of water velocity-induced errors is not considered. Finally, a direct ray-tracing approach is performed using an equal velocity of 1,500 m/s, calculated from the XBT data.

3.1. Seabed Detecting

Even though EK data can be used to study seabed characteristics (Preston et al., 2001), our study mainly focuses on its variation in the water column. Therefore, it is crucial to determine the sea bottom and extract data above it (Snellen et al., 2011). In this study, the cubic spline method was applied to calculate the upper envelopes of energy along the trace. The default energy value of the seabed signal for the instrument is defined to be -50 dB, as mentioned in its manual. We thus determined a slightly lower energy level of -55 dB to be the sea floor. By scanning the energy level from small to large water depths, we can avoid any possible effect originating from and beneath the sea floor. This method, calculating the energy envelope, avoids interference from the gentle slope and high-flux gas emission near the seabed, which can mislead our determination of the seafloor. Finally, we examined all the EK images to ensure that the seabed was well selected. The results show that the seabed can be determined most of the time (e.g., Figure 2c), except for two profiles in the FDV where a high bathymetric variation exists. In the high bathymetric variation areas, a relatively more extended footprint could induce a relatively minor amplitude and longer duration of the EK signal and cause difficulty in seabed determination.

3.2. Background Noise Estimation and Target Signal Detection

The background noise distribution could affect the detection of our targets. Therefore, it is essential to have a robust background noise evaluation that generally varies with depth. We calculate an average background noise level at different depths for each profile (black line on the right-hand side of Figure 2c). The focus of our study is the bubble signals that appeared in the water column. Therefore, the data of the bins located under the seabed were muted to avoid a miscalculation of the background noise level. Generally ranging from -140 to -80 dB, the acoustic background noise exhibits an inverse relationship with water depth, experiencing a gradual attenuation to -120 dB beyond a specific depth threshold which varying between 500 and 1,000 m across different locations and temporal instances. This variation may be related to the concentration of suspended particles in the water column. Through trial and error, we selected the areas with an energy level higher than -90 and 12 dB more significant than the average noise level of the depth to be the potential target signals (yellow and blue dots in Figure 2d). Then, we examined the energies of the adjacent grids located within five sampling points both in shooting numbers (horizontal distance) and time interval (vertical distance) of the acoustic profile to verify the signal continuity. When the number of adjacent grid points whose energy is in the target range is over a preset value, we identified their center as a selected signal point (blue dots in Figure 2d, the selected points). As the flare patterns are primarily similar for the profiles with similar mechanical angles (Figures 2a and 2b) and dependent occurrence (Figure 2c) (Velooso et al., 2015), the preset values are similar for the images acquired in the area. This preset value was determined by considering the shape and strength of the potential plume signals. Narrow or weak signals generally have a lower value. In our study, six was used as the default value in the program. By applying this procedure, we can avoid possible misinterpretation caused by energy outbursts and random noise, which are generally not linked to degassing activity. Then, we can use the information of the along- and athwart-ship angles to estimate the spatial distribution of the selected signal points (Jech et al., 2005; Sauter et al., 2006; Velooso et al., 2015; Wenau et al., 2018).

3.3. Source Intensity and Distribution

Precise source density estimation can help determine the magnitude of degassing effects. To determine the source density of the degassing activities and their distribution, it is important to define the source area. During the data acquisition experiments, almost all the traces for the EK data acquisition were aligned with the NNE–SSW direction to avoid the influence of the Kuroshio Current on the ship's attitude. Only 3 traces along the other direction were applied in the YK4-1, PFZ and GLM areas. The dense and subparallel survey traces provide a continuous spatial distribution of the gas flares and allow defining the source location. For example, gas flares without roots usually result from lateral and upward propagation (Figure 3a). After obtaining a more precise source location of the plumes on the seabed, we estimated the energy density of the source area by using the data points located within 30 m above the seabed. The selection of the data points at this depth range can help to avoid the influence of other factors in flare distribution, such as ocean currents or energy attenuation. The rising velocity

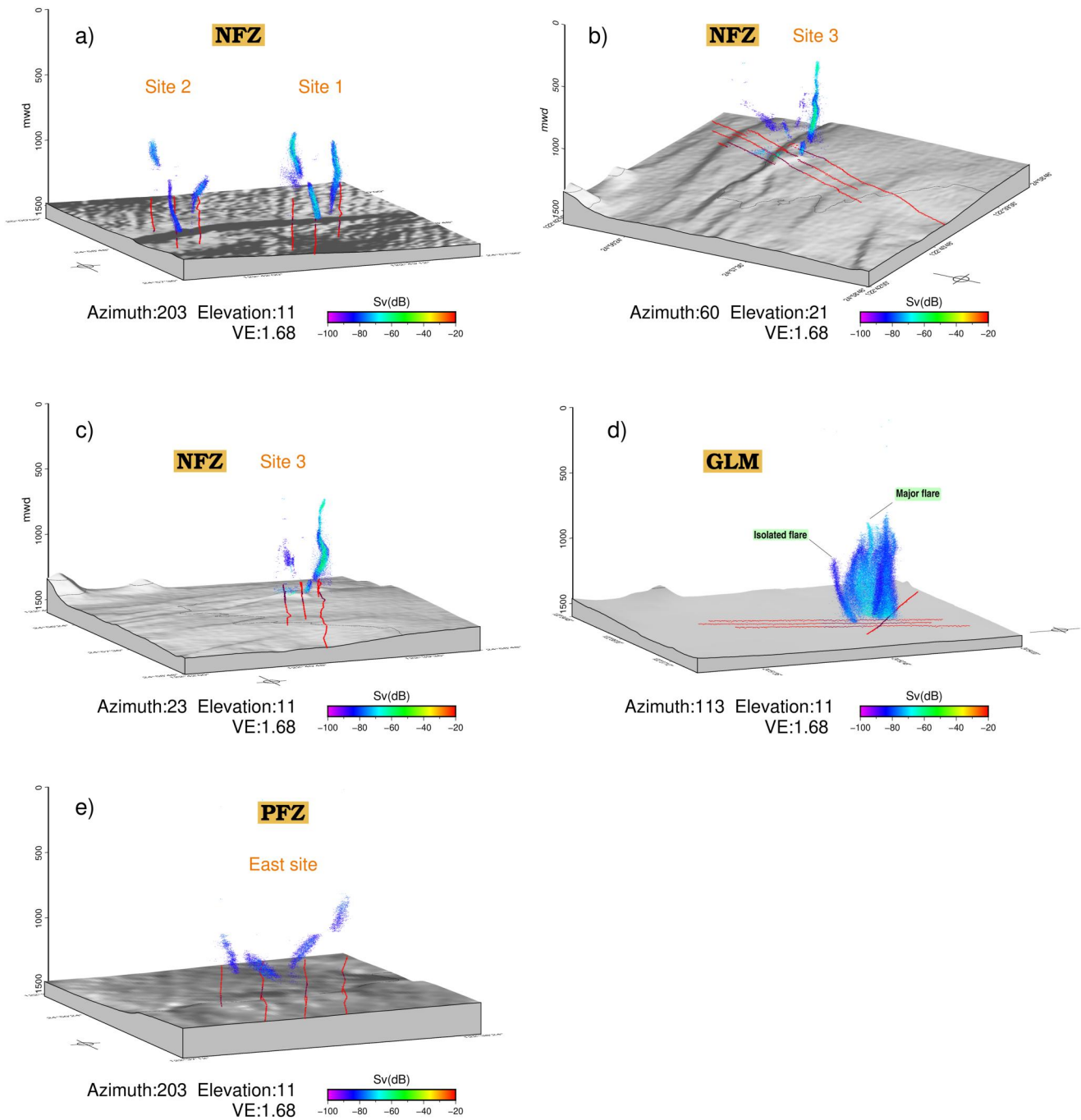


Figure 3. Three-dimensional visualization of the gas flares detected by using our software. (a) Two isolated flares with different energy strengths at site 1 and site 2 of the NFZ. Panels (b) and (c) show the gas flare at site 3 of the NFZ from different azimuths. (d) Gas flares images in the GLM. The isolated flare shows a lower energy magnitude and opposite rising direction compared to the major flare in the GLM. (e) Gas flares determined by the 4 adjacent survey lines east of the PFZ.

of the bubble is 47 cm/s on average from ROV images in YK4-1 (Chi, 2017; Wang, 2016), which is approximately 2 times that of NW-Svalbard (16.38 cm/s) (Veloso et al., 2015) and Congo (19 cm/s) (Wenau et al., 2018). This observation suggests that 1 minute of rising time would not cause a large deviation in the source area on the seafloor.

To better estimate the uncertainty in the source position determination, we calculated the 2-D standard deviation of the position between the selected points and the assumed source position for an isolated discharge event

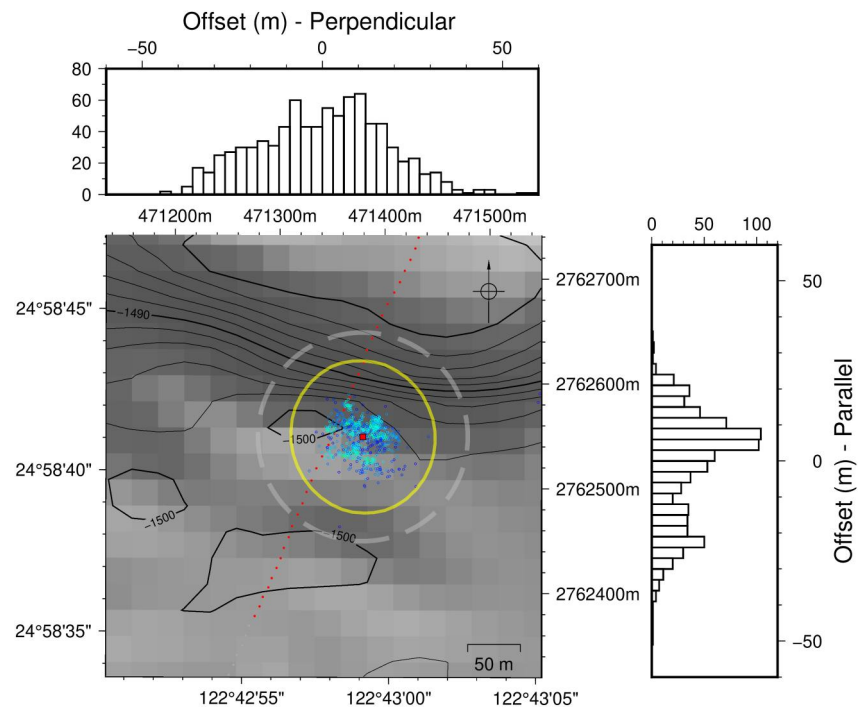


Figure 4. Distribution of data points within 30 m from the seabed of site 1 of the NFZ. Light and dark blue dots are the data points determined by our software, and the red square is the mean value of all the data points. The standard deviation for the distribution of data points is 24 m. The yellow circle indicates the KDE result, and the gray dashed circle shows the footprint at 1,500 mwd. Upper and right histograms show the distribution of data points perpendicular and parallel to the survey line.

(Figure 4), which is the median of all the data points. As the gas flare of Site 1 in the NFZ revealed a thin and continuous flare pattern (Figures 1 and 3a), we supposed it to be an isolated event and proceeded with related analysis. The calculation shows an average 2-D standard deviation of 24 m for the selected signal points. As the water depth in Site 1 of NFZ is approximately 1,500 m water depth (mwd), which is the deepest of our study area, we can thus assume that there are more minor errors for other survey sites, while their water depth is generally shallower. By comparing the offset distribution between the selected points and the assumed source position, we found a more significant standard deviation from the direction perpendicular to the survey line. This phenomenon may infer a relatively dominant ship roll effect. In addition, the two peaks identified from the track-parallel direction should be due to the changes in relative position between the ship and the object. Since the footprint increases as the water depth increases, we consider 24 m to be the maximal residual that this analysis can have.

In the next stage, we apply multivariate kernel density estimation to define the source boundary. This procedure was generally performed by the gridding method (Wenau et al., 2018). However, hydrothermal vents can generate multiple plumes (Nakamura et al., 2015), and the backscatter signal energy results from the superposition of multiple sources. Therefore, the density of the signal is highly sensitive to the placement of the reference point using the gridding method. The 2-D kernel density estimation (KDE) (Parzen, 1962; Rosenblatt, 1956; Spencer et al., 2017) can provide a more precise distribution when in the proper bandwidth. The method is commonly used to estimate the spatial distribution of affected areas for events of various scales or the probability of event occurrences (e.g., Connor et al., 2019; Woo, 1996).

The KDE is defined as follows:

$$f_H(x) = 1/n \sum_{i=1}^n K_H(x - x_i)$$

where $x = (x_1, x_2, \dots, x_d)^T$, $x_i = (x_{i1}, x_{i2}, \dots, x_{id})^T$, $i = 1, 2, \dots, n$. Here, $K(x)$ is the multivariate kernel, which we assume to be a round probability density function; H is the bandwidth matrix, which is symmetric and positive

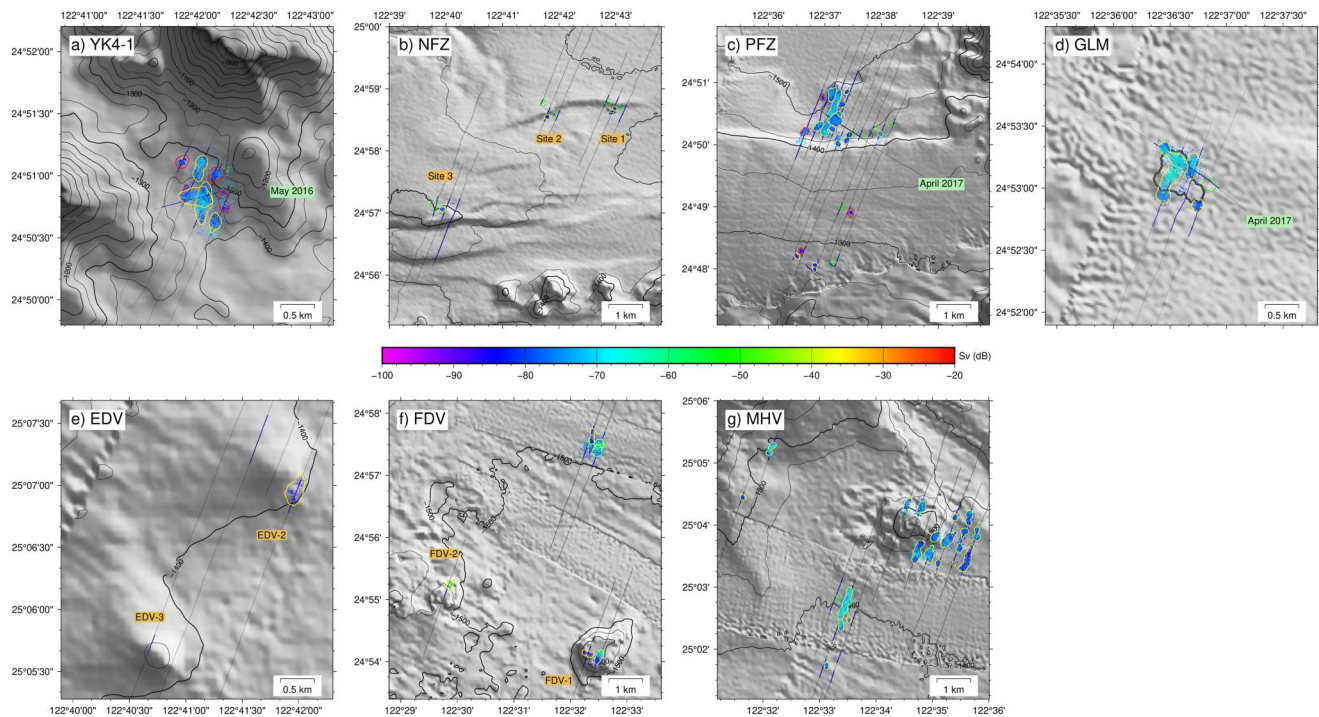


Figure 5. KDE distribution determined from the acoustic data points located within 30 m above the seafloor. Gray and blue lines indicate the survey profiles and bins in which the signals of flares were detected, respectively. Yellow contours mark areas of high Sv value, while red contours indicate weak energy areas. The green dashed contours show the bottom of rootless acoustic anomalies. The data points were projected onto the surface, and their value indicated the Sv value. The dark gray contour in (d) marks the knoll area detected from side-scan echo sounder observations.

definite, and the default value is 25 m, which is based on the standard deviation from the distribution; and $K_H(x) = |H|^{-\frac{1}{2}}K\left(H^{-\frac{1}{2}}x\right)$. By applying this procedure, we can estimate the density distribution and define the possible source boundary for different geological areas (Figure 4).

4. Results and Discussion

4.1. Gas Plume Distribution

The distribution of the KDE shows that the acoustic anomalies can be divided into two types: isolated and widely distributed anomalies (Figure 5) based on their scales. Isolated flares are smaller in scale, typically appearing only along a single survey profile. The range depicted by the KDE, highlighted by the yellow or red line in Figure 5, also approximates either a singular point or exhibits limited extended features. Most isolated flares are located along normal faults, such as in the NFZ (Figure 5b), east of the PFZ (Figure 5c), or near independent submarine volcanoes, such as in the FDV (Figure 5f) and EDV (Figure 5e). For the wide leakage area, YK4-1 is a typical example, where clustered hydrothermal vents have been discovered in a previous study (Figure 5a) (Matsumoto et al., 2001). A similar pattern was also determined in the GLM, in the western PHZ and in the MHV. Therefore, both types of flares were observed in the GLM (Figure 5d) and in the PFZ (Figure 5c).

Wide leakage areas are usually composed of multiple plumes. When the spacing between each flare is less than the instrument resolution, we observe continuous leakage patterns (e.g., the major flare in Figure 5d). Generally, the average Sv of the wide leakage is relatively higher, and a value of over -65 dB was observed for the major flares. In YK4-1 (Figure 5a), stronger emissions were recognized along the isocontour of 1,350 mwd and concentrated to an area of approximately 0.28 km^2 . Three major emissions, showing a N–S trending pattern, with a small gap between them, correspond to the observations performed by Konno et al. (2006). However, except for these major features, weaker emission activities also occurred on its eastern and northwestern sides at a relatively shallower water depth. Even though the YK4-1 site is not located at the top of any knoll, the area is characterized by numerous submarine volcanoes, named CVBT. Therefore, volcanic activity should be the origin of degassing

activity. The size and magnitude of the wide gas emission activity in GLM is similar to that in YK4-1, with a size of approximately 0.23 km² and an average intensity of approximately −65 dB. Except for the major continuous flares located in the western part of the area at approximately 1,500 mwd, an independent gas plume exists in its southeastern part. Hundreds of small knolls and visible gas plume signals in the water column over the GLM (black contour in Figure 5d) were reported by Tsai et al. (2021) from side-scan images. In our observations, extensive gas emission activity only occurred in the western part of the GLM, and the coexistence of gas plumes and knolls infers a causal relationship between them. Meanwhile, the major isolated plume is located at the border of the area. A wide and substantial plume area with a surface area of approximately 1.01 km² and an average energy density of −63 dB also extended west of the PFZ (Figure 5c) at a water depth of approximately 1,450 mwd. Unlike the gas plumes in YK4-1 and GLM, no knoll was reported in this area. However, marine geophysical data show an extensive presence of gas-enriched sedimentary layers (Hsu, 2017), which may explain the origin of this vast distribution of degassing activity. In the MHV area (Figure 5g), the impact of bad weather conditions was illustrated by poor data quality. Most profiles recorded deadlines and discontinued flares. The relatively larger spacing between the two profiles also caused insufficient coverage of the footprint. Nevertheless, the continuous along-profile distribution of gas flares illustrates the existence of massive degassing activity (2.52 km²) (Figure 5g). Due to the lack of broad-scale marine geophysical data, the geological structures and the nature of this degassing effect are not well known. However, active hydrothermal mounds have been reported by real-time seafloor observations (Chou et al., 2019), which infer strong hydrothermal potential around the area.

Three groups of isolated flares, one with a twisted form, were observed in the NFZ (Figure 5b). Two of the flares (site 1 and 2) were located along the normal N–E fault alignment, and the last flare (site 3) was located on the top of a knoll. At sites 1 and 2, no-root flares were observed on several profiles, revealing a lateral propagation process of the gas flares (Figure 3a). The position of the main flare (with root) can be traced based on the images of their adjacent profiles. The gap between them should result from the limitation of the footprint coverage of each single trace, which caused the shallow portion between the two profiles to not be well resolved. The Sv strength of the flare at site 1 (~−60 dB) is higher than that at site 2 (~−75 dB). At site 3, a major flare exists with the highest Sv value in the zone of approximately −52 dB, which propagates gradually from the seafloor to shallow water depths. Site 3 is located on top of the knoll, the core sampling image of site 1 shows sediment cavities due to gas hydrate dissociation, and the geochemical analysis detects a high concentration of methane near the seabed (Su, 2017). Both observations might explain their relatively stronger energy. Further to the south, several isolated gas plumes were also observed along the normal fault alignments in the PFZ (Figure 5c). Some scattered no root flares were observed in the PFZ area. An energy density of approximately −70 dB shows a similar energy density as for site 2 of the NFZ, which infers that all the gas plumes located along the normal faults possess similar magnitudes, except for sites 1 and 3 of the NFZ with stronger energy.

Unlike the rootless flares in the NFZ and PFZ, which extend from the main flare (i.e., flares with root) and can be observed on their adjacent profiles, only isolated rootless flares were recognized in EDV-2 and EDV-3 (Figure 5e). The former was characterized by energy (~−85 dB) relatively lower than the latter (~−65 dB). No flare was recorded on EDV-1 during the survey. In total, three survey lines passed across the EDV-2 knoll area. However, the flare signals were only recognized from two of them, the first and the third, not from the middle profile. This discrepancy could be induced by the difference in observation time. Around the EDV-2 volcano area, the flare was observed only in its southeastern slope with an energy level between −75 and −90 dB. Smog with relatively weaker intensity appears nearby along the seabed. High resolution, high-frequency, and close-attitude side-scan sonar images reveal a more detailed appearance of the smog in the water column (e.g., Kumagai et al., 2010; Tsai et al., 2021).

In the FDV-1 area (Figure 5f), a widespread flare, probably originating from the volcano center and propagating in the SSW direction, was observed. The acoustic profile acquired from its western side shows a rootless flare, which could result from the westward propagation of the flare. In FDV-2, the flare was located on the NE slope of a knoll. The magnitude of the energy level is smaller than that observed in FDV-1. To the north of the FDV area, a high-energy flares area appears (Figure 5f). However, the lack of precise bathymetry data hinders the understanding of its mechanism, even though the strength is relatively high (~−53 dB). Overall, the density of the flares observed in the FDV group is much higher than that observed around the normal faulting area, with an average of approximately −55 dB. Due to unfavorable weather conditions and wider line spacing, accurately mapping the extensive yet sporadic distribution of the KDE in the southwest of MHV (Figure 5g) remains a challenge.

However, relying on additional seabed observation data, we posit that this region continues to be a significant area for gas discharge on a large scale.

Based on our observations, we found that widespread gas flares usually occurred in areas where there was large-scale volcanic activity or gas-enriched structures, such as YK4-1 and GLM for the former and the northern part of the PFZ for the latter. Isolated gas plumes could be found for a single knoll outcrop and normal faulting structures, such as the FDV group for the former and the NFZ and southern PFZ group for the latter. However, the energy flux of the flares in the knoll area is generally stronger than those observed along the normal faults. In the area where buried volcanic rock exists, relatively weaker gas plume activity was also reported. In 2016 and 2017, four types of deep-towed vehicles were used to collect underwater optical imagery on YK4-1, PFZ, MHV, FDV-1, and GLM (Chou et al., 2019). Hydrothermal fluid activities were mapped for many potential sites. Comparing the areas observed from optical imagery and the KDE distribution, only the fluid activity distinguished in the northern GLM was not reflected by the KDE distribution. This observation suggests that the composition of the fluid activity may be too pure to generate a backscattering effect and to be recorded by the EK system around the GLM. Another possibility is that the discharges are intermittent, with no activity during the observation period.

As mentioned previously, the EK profiles were collected in 2016 and 2017. All the survey lines performed in 2016 trend along the NNE–SSW direction, while those acquired in 2017 have different orientations. Thus, by comparing the images of these profiles from different times, we analyzed the time evolution of the gas flares for the YK4-1, PFZ and GLM sites (Figure 5). Overall, even though the gas distribution patterns are slightly different, the results obtained from the different year surveys show that the discharge is roughly stable (Figures 5a, 5c and 5d).

4.2. 3-D Gas Flare Structures

In our study, except for the determination of gas plume source areas and the energy estimation, the 3-D gas plume images, obtained by calibrating with the ship attitude, give us the opportunity to further analyze the flares structures (Figure 3). We found that the position of the most widely extended flares did not vary with depth, and they often show straight-up patterns (Figure 3d). This distribution pattern may be caused by the relatively high gas plume energy and/or a higher bubble rising rate. However, we can still observe some lateral flare propagation near these extensive degassing zones, such as in the eastern part of the GLM, where only rootless plumes were observed (Figure 3d). Most of the isolated flares show a tilted upward migration path, which can also be expressed by the rootless flares on the adjacent profiles of the main gas plume source, such as those observed in the PFZ, NFZ and EDV (Figures 3a and 3c). Tsai et al. (2019) considered that rootless flares result from intermittent discharges caused by tidal-induced pressure changes and intermittent discharges (Su, 2017; e.g., Hsu et al., 2013; Marcon et al., 2021). However, the 3-D gas plume distribution demonstrates that lateral propagation might better explain the phenomenon. Thus, compared to the traditional 2-D acoustic survey results, the 3-D distribution of flares provides more spatial relevance of the images between the adjacent profiles. The influence of bottom currents is thought to be the cause of this lateral migration of gas plumes while rising. By following the trend of the rootless plumes, we can generally trace their source area. We found that the gas plumes could have different lateral propagation directions even though the source area appears to be identical. Figure 3e shows one example of flare propagation in the PFZ area. The individual flare, located at approximately 122°37'75"E and 24°50'12"N, shows a drastic change in direction that turns from the northeast to the southeast (Figure 6): the former occurred during the flood tide, while the latter occurred during the ebb tide (insert figure in Figure 6). It is worth noting that the tidal current seems to drag the gas plume far away from land during the flood tide and vice versa, which is different from the general concept. Both directions trend along a similar bathymetry depth, which corresponds to the foot of the OT southern slope. This observation shows that the flare distribution could be an indicator for the water mass migration caused by the tidal flow. Therefore, the slope-parallel flare features suggest that topography is also a main factor controlling the deep-sea current (Mitsuzawa & Holloway, 1998).

Furthermore, we observed that the shapes and energy level of the 3-D gas plumes usually vary with depth. For example, at site 3 of the NFZ, a major flare originating from the seafloor with a high Sv value of approximately –52 dB propagates gradually to shallow water depths, and its width expands gradually at depths between 900 and 1,400 mwd (Figures 3b and 3c). The flare pattern becomes thinner but still has high energy while moving upward to 650 mwd. The distinct spreading of the gas flare at certain depths could be due to the neutral buoyancy, which means that the gas bubbles may achieve a force balance state and maintain their position. We also noticed that no

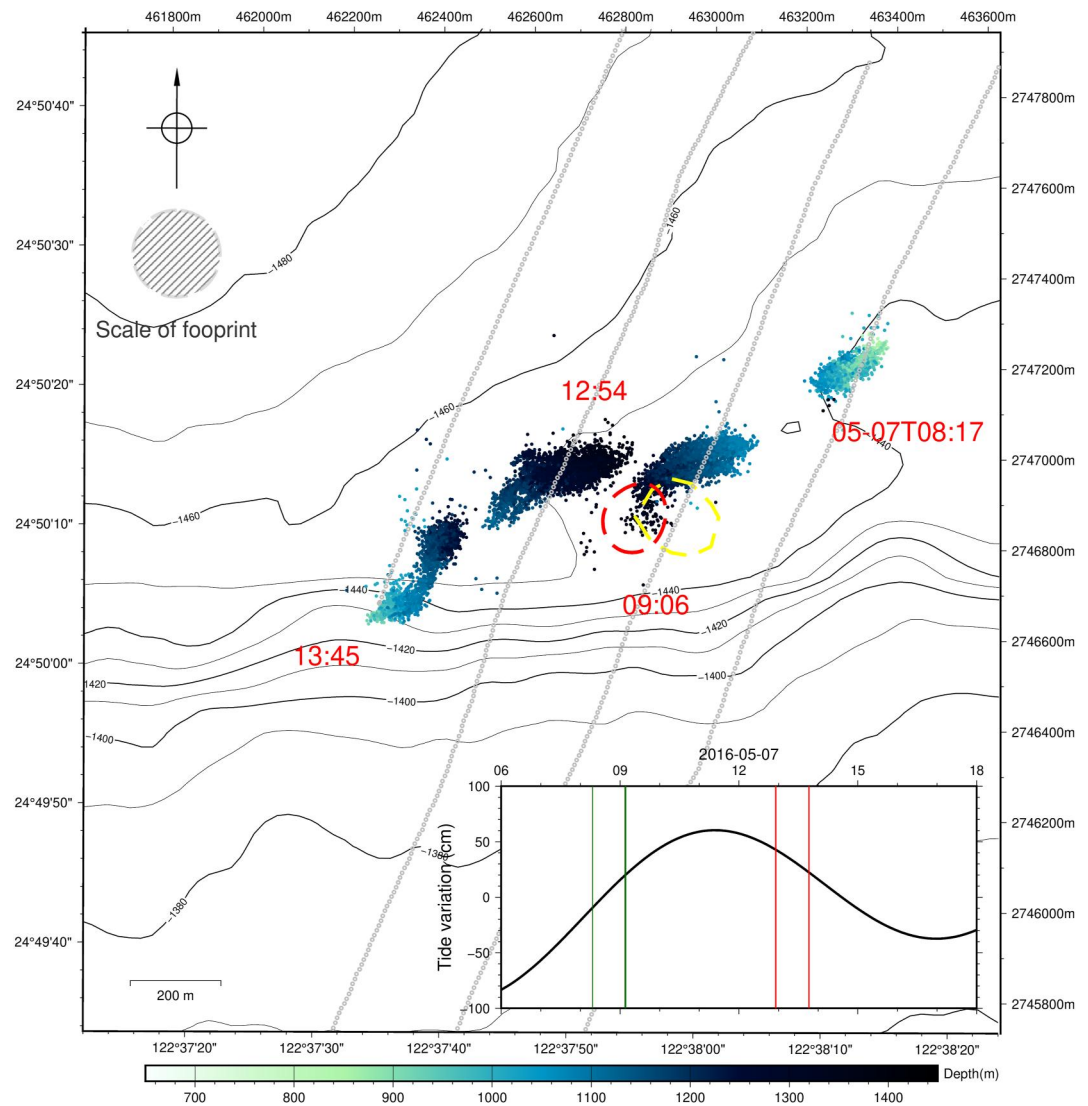


Figure 6. Plane distribution of the data points observed in the eastern PFZ. The color of the dots shows the water depth of the observed data points. Diagonal hachure pattern in the upper left corner indicates the scale of footprint in 1,450 mwd. Very dense pattern of small gray dots forms the survey traces. Yellow and red dashed contours mark the KDE determined before and after the removal of points with better quality. The inset figure shows the tidal variation in the vicinity area. Dark green and red lines indicate the timing for the four survey lines. The gas flares observed during the period marked by the green lines migrate toward the NE direction, while those during the period marked by the red lines migrate toward the opposite direction. The tide variation is calculated with the tidal prediction system NAO.99b (Matsumoto et al., 2000).

gas flare can be observed when the water depth is shallower than 500–700 mwd. This phenomenon could be due to the dissolution of gas bubbles in the water column, which is generally controlled by the physical properties of bubbles, such as their sizes and compositions. Konno et al. (2006) determined the chemical and isotopic compositions of liquid carbon dioxide from the YK4-1 site and discovered that liquid carbon dioxide was mostly derived from hydrothermal fluid. The carbon dioxide bubbles rise upward in the water column, and their hydro skin can retard the bubble dissolution procedure. When the rising bubble touches the bottom of the thermocline layer, which is approximately 500–700 mwd, the bubble will dissolve into the water quickly (Bigalke et al., 2008; Nakamura et al., 2015). Therefore, the shallowest water depth of the carbon dioxide bubble with hydro skin is usually at approximately 500 mwd. This phenomenon could explain the fact that most of the gas flares disappear at similar water depths in our observations. However, other factors, such as background noise level and instrument detection capability, can also affect the flares patterns. The high background noise at depths shallower than 900 mwd, probably caused by thermocline or ocean current, could drown out the flare signals with weaker

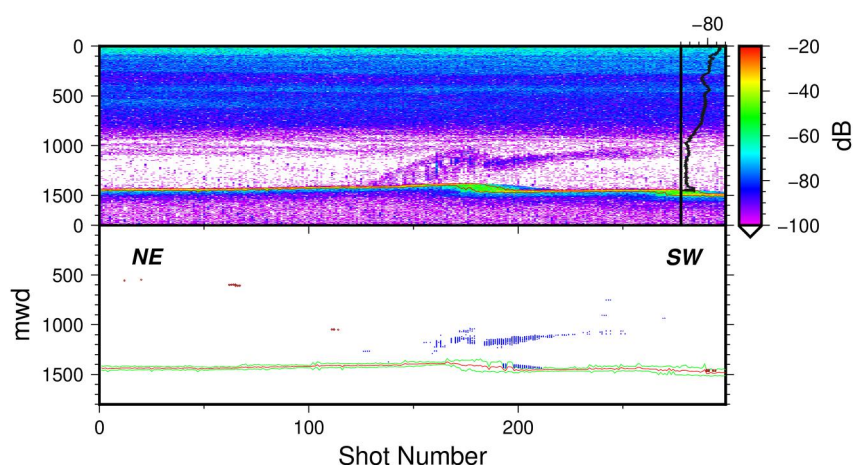


Figure 7. The Sv profile records a slight and narrow flare southeast of site 3 in the NFZ. The echogram record shows the rising plume depositing the mineral along the bottom of the thermocline by intrusion flow (Schneider von Deimling et al., 2015).

strength. In addition, the resolution for signal detection at shallow water portions could also be affected by footprint variation. Generally, only the images located around the central axis of the profiles can be well revealed at all depth ranges.

Even though the software allows a better illustration of the gas flares, we still need to mention some existing constraints that may influence our interpretation. First, nontargeted signals, such as the signal caused by plankton activity (Figure 2c) and ocean currents, may generate undesirable noise. However, this kind of signal usually has fixed specifications, such as the depth of occurrence and the frequency, and can be filtered out by programming. On the other hand, dramatic seafloor morphological changes, including landslides or gas-bearing layers, may cause a mixture of near-surface points and decrease the accuracy of seabed determination. This phenomenon influences the distribution of KDE (Figure 7) and affects the evaluation of the source area. The perturbation caused by this noise is generally weak and easy to remove. However, as this kind of feature happens irregularly, manual checking and removal are still needed. Another factor that can limit the accuracy of KDE is the footprint coverage of the instrument, as shown by our data acquired in the eastern part of the PFZ (Figure 6). The source is estimated to be between two survey profiles (Figure 6), and the image of the flares shows a slight connection to the seabed. Based on the KDE distribution obtained by the different data points, the root of the flares is offset by tens of meters. This gap may be generated by inconsistency between the heading direction of the GPS navigation and the yaw of the ship attitude while the survey line direction and/or weather condition change. On the other hand, footprint overlap can also affect Sv estimation (Velooso et al., 2015). When the distance from different discharge systems is smaller than the footprint, the different systems may be detected as one system and vary the Sv distribution evaluation. The deeper the water depth is, the larger the effect that footprint overlapping can induce. In a previous study, the intensity of Sv was used to qualify the erupting level of the gas emission or to determine its characteristics, such as the bubble diameter (Clay & Medwin, 1977; Kubilius & Pedersen, 2016), state of the bubble shell (Tishchenko et al., 2005), number of bubbles per unit volume, and response of the sonar frequency (Kubilius & Pedersen, 2016). However, our results show that related parameters should still be calibrated before conducting more sophisticated research.

5. Conclusions

In this study, we established software and developed a new EK data processing procedure to systematically integrate the widespread EK data and extract the 3-D gas plume characteristics, which allows a better investigation of the degassing mechanisms in the marine environment. After examining the 3-D images and the KDE constraint of the near-surface sources, 4 high-flux areas and 22 isolated plumes with roots were detected in this study. We found that widespread gas flares usually occurred in areas with large-scale volcanic activity or gas-enriched structures, such as YK4-1, GLM and the northern part of the PFZ. The comparison between the side-scan echo sounder images and the KDE distribution estimated from this study around the GLM demonstrates a high degree of coincidence between the presence of knolls and a high KDE value area. We suggest that the

widespread distribution of gas flares may infer a larger hydrothermal potential, which could not be revealed by a single acoustic image profile observation. Isolated gas plumes could be found near the single knoll outcrop and normal faulting structures, such as the FDV group, the NFZ, and the southern PFZ group. The energy flux of the flares around the knoll area is generally stronger than those observed along the normal faults. Although the survey tracks performed for different time spans are few, the gas flares distribution of 2016 and 2017 is similar, which may indicate that the gas discharge is stable in this area. Except for a higher accuracy for the source determination, the tidal fluctuation and the seawater depth-dependent variation could also be evaluated based on the 3-D visualization of isolated flares. The maximal height that the flares can attain may represent the boundary of the thermocline, where the bubbles compositing carbon dioxide dissolve.

Data Availability Statement

Version 1.0.0 of the ek60-3D used for reading EK60 data and calculating three-dimensional point cloud distribution is preserved at <https://doi.org/10.5281/zenodo.8089478> (Y.-C. Lin, 2023) available via CC-BY and published on GitHub <https://github.com/ray265/ek60-3D>. All requests for materials in this paper should be addressed to Jing-Yi Lin (jylin.gep@gmail.com).

Acknowledgments

The study was supported by the geological investigation of mineral resource potential offshore northeastern Taiwan project awarded by the Central Geological Survey (CGS), Ministry of Economic Affairs, Taiwan. We are appreciated the assistance of the crew of R/V Ocean Researcher II in collecting data. We express our gratitude for the valuable comments provided by reviewer Dr. Hidenori Kumagai during the review process.

References

- Bigalke, N. K., Rehder, G., & Gust, G. (2008). Experimental investigation of the rising behavior of CO₂ droplets in seawater under hydrate-forming conditions. *Environmental Science and Technology*, 42(14), 5241–5246. <https://doi.org/10.1021/es800228j>
- Chen, S.-C., Lin, J.-Y., Su, C.-C., & Doo, W.-B. (2019). Introduction to the special issue on tectonic environment and seabed resources of the southern Okinawa Trough. *Terrestrial, Atmospheric and Oceanic Sciences*, 30(5), 605–611. <https://doi.org/10.3319/tao.2019.08.27.01>
- Chi, W.-C. (2017). *Geological Investigation of Mineral Resource Potential in the Offshore Northeastern Taiwan: Fluid migration modeling in the mineral resource potential area (2/4)* (Vol. 106–12-C, p. 45). Report of Central Geological Survey. Retrieved from <https://www.grb.gov.tw/search/planDetail?id=12087579>
- Chou, Y.-C., Wang, C.-C., Chen, H.-H., & Lin, Y.-H. (2019). Seafloor characterization in the southernmost Okinawa Trough from underwater optical imagery. *Terrestrial, Atmospheric and Oceanic Sciences*, 30(5), 717–737. <https://doi.org/10.3319/tao.2019.03.14.01>
- Chung, S.-L., Wang, S.-L., Shinjo, R., Lee, C.-S., & Chen, C.-H. (2000). Initiation of arc magmatism in an embryonic continental rifting zone of the southernmost part of Okinawa Trough. *Terra Nova*, 12(5), 225–230. <https://doi.org/10.1046/j.1365-3121.2000.00298.x>
- Clay, C. S., & Medwin, H. (1977). *Acoustical oceanography: Principles and applications*. Wiley. Book.
- Connor, C. B., Connor, L. J., Germa, A., Richardson, J. A., Bebbington, M. S., Gallant, E., & Saballos, A. (2019). How to use kernel density estimation as a diagnostic and forecasting tool for distributed volcanic vents. *Statistics in Volcanology*, 4(1), 3–25. <https://doi.org/10.5038/2163-338X.4.3>
- Doo, W.-B., Hsu, S.-K., Wang, H.-F., Huang, Y.-S., Tsai, C.-H., Lo, C.-L., et al. (2019). A deep-towed magnetic survey in the southern Okinawa Trough: Implications for hydrothermal system detection. *Terrestrial, Atmospheric and Oceanic Sciences*, 30(5), 675–683. <https://doi.org/10.3319/tao.2019.02.15.01>
- Gena, K., Chiba, H., Kase, K., Nakashima, K., & Ishiyama, D. (2013). The Tiger sulfide chimney Yonaguni Knoll IV hydrothermal field, southern Okinawa Trough, Japan: The first reported occurrence of Pt-Cu-Fe-bearing bismuthinite and Sn-bearing chalcopyrite in an active seafloor hydrothermal system. *Resource Geology*, 63(4), 360–370. <https://doi.org/10.1111/rge.12015>
- Glasby, G. P., & Notsu, K. (2003). Submarine hydrothermal mineralization in the Okinawa Trough SW of Japan: An overview. *Ore Geology Reviews*, 23(3–4), 299–339. <https://doi.org/10.1016/j.oregeorev.2003.07.001>
- Halbach, P., Nakamura, K., Wahsner, M., Lange, J., Sakai, H., Käselitz, L., et al. (1989). Probable modern analogue of Kuroko-type massive sulphide deposits in the Okinawa Trough back-arc basin. *Nature*, 338(6215), 496–499. <https://doi.org/10.1038/338496a0>
- Hsu, H.-H., Lin, L.-F., Liu, C.-S., Chang, J.-H., Liao, W.-Z., Chen, T.-T., et al. (2019). Pseudo-3D seismic imaging of Geolin Mounds hydrothermal field in the Southern Okinawa Trough offshore NE Taiwan. *Terrestrial, Atmospheric and Oceanic Sciences*, 30(5), 705–716. <https://doi.org/10.3319/tao.2019.03.14.02>
- Hsu, S.-K. (2017). *Geological Investigation of Mineral Resource Potential in the Offshore Northeastern Taiwan: High-resolution Sonar and Magnetic Surveys (2/4)* (Vol. 106–13, p. 237). Report of Central Geological Survey. Retrieved from <https://www.grb.gov.tw/search/planDetail?id=12080555>
- Hsu, S. K., Wang, S. Y., Liao, Y. C., Yang, T. F., Jan, S., Lin, J. Y., & Chen, S. C. (2013). Tide-modulated gas emissions and tremors off SW Taiwan. *Earth and Planetary Science Letters*, 369, 98–107. <https://doi.org/10.1016/j.epsl.2013.03.013>
- Huang, Y.-S., Su, C.-C., Doo, W.-B., Hsu, S.-K., Tsai, C.-H., Wang, H.-F., et al. (2019). Hydrothermal activity revealed by rock magnetic anomaly from core sediments in the southern Okinawa Trough. *Terrestrial, Atmospheric and Oceanic Sciences*, 30(5), 685–694. <https://doi.org/10.3319/tao.2019.07.31.01>
- Inagaki, F., Nunoura, T., Nakagawa, S., Teske, A., Lever, M., Lauer, A., et al. (2006). Biogeographical distribution and diversity of microbes in methane hydrate-bearing deep marine sediments on the Pacific Ocean Margin. *Proceedings of the National Academy of Sciences*, 103(8), 2815–2820. <https://doi.org/10.1073/pnas.0511033103>
- Ishibashi, J.-I., Noguchi, T., Toki, T., Miyabe, S., Yamagami, S., Onishi, Y., et al. (2014). Diversity of fluid geochemistry affected by processes during fluid upwelling in active hydrothermal fields in the Izena Hole the middle Okinawa Trough back-arc basin. *Geochemical Journal*, 48(4), 357–369. <https://doi.org/10.2343/geochemj.2.0311>
- Ishibashi, J., Ikegami, F., Tsuji, T., & Urabe, T. (2014). *Hydrothermal activity in the Okinawa Trough back-arc basin: Geological background and hydrothermal mineralization*. In *Subseafloor Biosphere Linked to Hydrothermal Systems* (pp. 337–359). Springer. https://doi.org/10.1007/978-4-431-54865-2_27
- Jech, J. M., Foote, K. G., Chu, D., & Hufnagle, L. C. (2005). Comparing two 38-kHz scientific echosounder. *ICES Journal of Marine Science*, 62(6), 1168–1179. <https://doi.org/10.1016/j.icesjms.2005.02.014>

- Jerram, K., Weber, T. C., & Beaudoin, J. (2015). Split-beam echo sounder observations of natural methane seep variability in the northern Gulf of Mexico. *Geochemistry, Geophysics, Geosystems*, 16(3), 736–750. <https://doi.org/10.1002/2014gc005429>
- Kimura, M. (1985). Back-arc rifting in the Okinawa Trough. *Marine and Petroleum Geology*, 2(3), 222–240. [https://doi.org/10.1016/0264-8172\(85\)90012-1](https://doi.org/10.1016/0264-8172(85)90012-1)
- Kimura, M., Uyeda, S., Kato, Y., Tanaka, T., Yamano, M., Gamo, T., et al. (1988). Active hydrothermal mounds in the Okinawa Trough backarc basin Japan. *Tectonophysics*, 145(3–4), 319–324. [https://doi.org/10.1016/0040-1951\(88\)90203-x](https://doi.org/10.1016/0040-1951(88)90203-x)
- Klingelhoefer, F., Lee, C.-S., Lin, J.-Y., & Sibuet, J.-C. (2009). Structure of the southernmost Okinawa Trough from reflection and wide-angle seismic data. *Tectonophysics*, 466(3–4), 281–288. <https://doi.org/10.1016/j.tecto.2007.11.031>
- Konno, U., Tsunogai, U., Nakagawa, F., Nakaseama, M., Ishibashi, J., Nunoura, T., & Nakamura, K. (2006). Liquid CO₂ venting on the seafloor: Yonaguni Knoll IV hydrothermal system, Okinawa Trough. *Geophysical Research Letters*, 33(16). <https://doi.org/10.1029/2006gl026115>
- Kubilius, R., & Pedersen, G. (2016). Relative acoustic frequency response of induced methane carbon dioxide and air gas bubble plumes, observed laterally. *Journal of the Acoustical Society of America*, 140(4), 2902–2912. <https://doi.org/10.1121/1.4964250>
- Kumagai, H., Tsukioka, S., Yamamoto, H., Tsuji, T., Shitashima, K., Asada, M., et al. (2010). Hydrothermal plumes imaged by high-resolution side-scan sonar on a cruising AUV, Urashima. *Geochemistry, Geophysics, Geosystems*, 11(12). <https://doi.org/10.1029/2010gc003337>
- Lee, C.-S., Shor, G. G., Bibee, L. D., Lu, R. S., & Hilde, T. W. C. (1980). Okinawa Trough: Origin of a back-arc basin. *Marine Geology*, 35(1–3), 219–241. [https://doi.org/10.1016/0025-3227\(80\)90032-8](https://doi.org/10.1016/0025-3227(80)90032-8)
- Letouzey, J., & Kimura, M. (1986). The Okinawa Trough: Genesis of a back-arc basin developing along a continental margin. *Tectonophysics*, 125(1–3), 209–230. [https://doi.org/10.1016/0040-1951\(86\)90015-6](https://doi.org/10.1016/0040-1951(86)90015-6)
- Lin, J.-Y., Hsu, S.-K., & Sibuet, J.-C. (2004). Melting features along the Ryukyu slab tear beneath the southwestern Okinawa Trough. *Geophysical Research Letters*, 31(19). <https://doi.org/10.1029/2004gl020862>
- Lin, Y.-C. (2023). ek60-3D (Version v1.0.0) [Computer software]. *Zenodo*. <https://doi.org/10.5281/ZENODO.8089478>
- Luders, V., & Niedermann, S. (2010). Helium isotope composition of fluid inclusions hosted in massive sulfides from modern submarine hydrothermal systems. *Economic Geology*, 105(2), 443–449. <https://doi.org/10.2113/gsecongeo.105.2.443>
- Marcon, Y., Kelley, D., Thornton, B., Manalang, D., & Bohrmann, G. (2021). Variability of natural methane bubble release at Southern Hydrate Ridge. *Geochemistry, Geophysics, Geosystems*, 22(10), e2021GC009894. <https://doi.org/10.1029/2021GC009894>
- Matsumoto, K., Takanezawa, T., & Ooe, M. (2000). Ocean tide models developed by assimilating TOPEX/POSEIDON altimeter data into hydrodynamical model: A global model and a regional model around Japan. *Journal of Oceanography*, 56(5), 567–581. <https://doi.org/10.1023/a:1011157212596>
- Matsumoto, T., Kinoshita, M., Nakamura, M., Sibuet, J.-C., Lee, C.-S., Hsu, S.-K., et al. (2001). Volcanic and hydrothermal activities and possible segmentation of the axial rifting in the westernmost part of the Okinawa Trough - Preliminary results from the YOKOSUKA/SHINKAI 6500 Lequios Cruise (No. 19). *Jamstec Journal of Deep Sea Research*, 95–107.
- Miki, M. (1995). Two-phase opening model for the Okinawa Trough inferred from paleomagnetic study of the Ryukyu arc. *Journal of Geophysical Research: Solid Earth*, 100(B5), 8169–8184. <https://doi.org/10.1029/95jb00034>
- Minami, H., & Ohara, Y. (2017). The Gondou hydrothermal field in the Ryukyu Arc: A huge hydrothermal system on the flank of a caldera volcano. *Geochemistry, Geophysics, Geosystems*, 18(9), 3489–3516. <https://doi.org/10.1002/2017gc006868>
- Mitsuzawa, K., & Holloway, G. (1998). Characteristics of deep currents along trenches in the northwest Pacific. *Journal of Geophysical Research*, 103(C6), 13085–13092. <https://doi.org/10.1029/97JC03416>
- Nakamura, K., Kawagucci, S., Kitada, K., Kumagai, H., Takai, K., & Okino, K. (2015). Water column imaging with multibeam echo-sounding in the mid-Okinawa Trough: Implications for distribution of deep-sea hydrothermal vent sites and the cause of acoustic water column anomaly. *Geochemical Journal*, 49(6), 579–596. <https://doi.org/10.2343/geochemj.2.0387>
- Nunoura, T., Oida, H., Nakaseama, M., Kosaka, A., Ohkubo, S. B., Kikuchi, T., et al. (2010). Archaeal diversity and distribution along thermal and geochemical gradients in hydrothermal sediments at the Yonaguni Knoll IV hydrothermal field in the Southern Okinawa Trough. *Applied and Environmental Microbiology*, 76(4), 1198–1211. <https://doi.org/10.1128/aem.00924-09>
- Park, J.-O., Tokuyama, H., Shinohara, M., Suyehiro, K., & Taira, A. (1998). Seismic record of tectonic evolution and backarc rifting in the southern Ryukyu island arc system. *Tectonophysics*, 294(1–2), 21–42. [https://doi.org/10.1016/s0040-1951\(98\)00150-4](https://doi.org/10.1016/s0040-1951(98)00150-4)
- Parzen, E. (1962). On estimation of a probability density function and mode. *The Annals of Mathematical Statistics*, 33(3), 1065–1076. <https://doi.org/10.1214/aoms/1177704472>
- Preston, J. M., Christney, A. C., Bloomer, S. F., & Beaudet, I. L. (2001). *Seabed classification of multibeam sonar images*. In *MTS/IEEE Oceans 2001. An Ocean Odyssey. Conference Proceedings (IEEE Cat. No.01CH37295)*. Marine Technol. Soc. <https://doi.org/10.1109/oceans.2001.968411>
- Römer, M., Sahling, H., Pape, T., Bohrmann, G., & Spieß, V. (2012). Quantification of gas bubble emissions from submarine hydrocarbon seeps at the Makran continental margin (offshore Pakistan). *Journal of Geophysical Research*, 117(C10), n/a–n/a. <https://doi.org/10.1029/2011jc007424>
- Rosenblatt, M. (1956). Remarks on some nonparametric estimates of a density function. *The Annals of Mathematical Statistics*, 27(3), 832–837. <https://doi.org/10.1214/aoms/1177728190>
- Sakai, H., Gamo, T., Kim, E.-S., Shitashima, K., Yanagisawa, F., Tsutsumi, M., et al. (1990). Unique chemistry of the hydrothermal solution in the mid-Okinawa Trough Backarc Basin. *Geophysical Research Letters*, 17(12), 2133–2136. <https://doi.org/10.1029/g1017i012p02133>
- Sauter, E. J., Muyakshin, S. I., Charlou, J.-L., Schlüter, M., Boetius, A., Jerosch, K., et al. (2006). Methane discharge from a deep-sea submarine mud volcano into the upper water column by gas hydrate-coated methane bubbles. *Earth and Planetary Science Letters*, 243(3–4), 354–365. <https://doi.org/10.1016/j.epsl.2006.01.041>
- Schneider von Deimling, J., Linke, P., Schmidt, M., & Rehder, G. (2015). Ongoing methane discharge at well site 22/4b (North Sea) and discovery of a spiral vortex bubble plume motion. *Marine and Petroleum Geology*, 68, 718–730. <https://doi.org/10.1016/j.marpetgeo.2015.07.026>
- Schneider von Deimling, J., Rehder, G., Greinert, J., McGinnis, D. F., Boetius, A., & Linke, P. (2011). Quantification of seep-related methane gas emissions at Tommeliten North Sea. *Continental Shelf Research*, 31(7–8), 867–878. <https://doi.org/10.1016/j.csr.2011.02.012>
- Shinjo, R., Chung, S.-L., Kato, Y., & Kimura, M. (1999). Geochemical and Sr-Nd isotopic characteristics of volcanic rocks from the Okinawa Trough and Ryukyu Arc: Implications for the evolution of a young intracontinental back arc basin. *Journal of Geophysical Research: Solid Earth*, 104(B5), 10591–10608. <https://doi.org/10.1029/1999jb900040>
- Sibuet, J.-C., Deffontaines, B., Hsu, S.-K., Thareau, N., Formal, J.-P. L., & Liu, C.-S. (1998). Okinawa Trough backarc basin: Early tectonic and magmatic evolution. *Journal of Geophysical Research: Solid Earth*, 103(B12), 30245–30267. <https://doi.org/10.1029/98jb01823>
- Sibuet, J.-C., Letouzey, J., Barbier, F., Charvet, J., Foucher, J.-P., Hilde, T. W. C., et al. (1987). Back arc extension in the Okinawa Trough. *Journal of Geophysical Research: Solid Earth*, 92(B13), 14041–14063. <https://doi.org/10.1029/jb092ib13p14041>

- Snellen, M., Siemes, K., & Simons, D. G. (2011). Model-based sediment classification using single-beam echosounder signals. *Journal of the Acoustical Society of America*, *129*(5), 2878–2888. <https://doi.org/10.1121/1.3569718>
- Spencer, C. J., Yakymchuk, C., & Ghaznavi, M. (2017). Visualising data distributions with kernel density estimation and reduced chi-squared statistic. *Geoscience Frontiers*, *8*(6), 1247–1252. <https://doi.org/10.1016/j.gsf.2017.05.002>
- Su, C.-C. (2017). *Geological Investigation of Mineral Resource Potential in the Offshore Area of Northeastern Taiwan: Geochemical investigation and sea floor imaging (2/4)* (Vol. 106–14-A, p. 239). Report of Central Geological Survey. Retrieved from <https://www.grb.gov.tw/search/planDetail?id=12079194>
- Suzuki, R., Ishibashi, J.-I., Nakaseama, M., Konno, U., Tsunogai, U., Gena, K., & Chiba, H. (2008). Diverse range of mineralization induced by phase separation of hydrothermal fluid: Case study of the Yonaguni Knoll IV hydrothermal field in the Okinawa Trough back-arc basin. *Resource Geology*, *58*(3), 267–288. <https://doi.org/10.1111/j.1751-3928.2008.00061.x>
- Tishchenko, P., Hensen, C., Wallmann, K., & Wong, C. S. (2005). Calculation of the stability and solubility of methane hydrate in seawater. *Chemical Geology*, *219*(1–4), 37–52. <https://doi.org/10.1016/j.chemgeo.2005.02.008>
- Toki, T., Itoh, M., Iwata, D., Ohshima, S., Shinjo, R., Ishibashi, J., et al. (2016). Geochemical characteristics of hydrothermal fluids at Hatoma Knoll in the southern Okinawa Trough. *Geochemical Journal*, *50*(6), 493–525. <https://doi.org/10.2343/geochemj.2.0449>
- Tsai, C.-H., Hsu, S.-K., Chen, S.-C., Wang, S.-Y., Lin, L.-K., Huang, P.-C., et al. (2021). Active tectonics and volcanism in the southernmost Okinawa Trough back-arc basin derived from deep-towed sonar surveys. *Tectonophysics*, *817*, 229047. <https://doi.org/10.1016/j.tecto.2021.229047>
- Tsai, C.-H., Hsu, S.-K., Chen, Y.-F., Lin, H.-S., Wang, S.-Y., Chen, S.-C., et al. (2019). Gas plumes and near-seafloor bottom current speeds of the southernmost Okinawa Trough determined from echo sounders. *Terrestrial, Atmospheric and Oceanic Sciences*, *30*(5), 649–674. <https://doi.org/10.3319/tao.2019.07.07.01>
- Uyeda, S. (1987). Active hydrothermal mounds in the Okinawa back-arc trough. *Eos Transactions American Geophysical Union*, *68*(36), 737. <https://doi.org/10.1029/eo068i036p00737-01>
- Veloso, M., Greinert, J., Mienert, J., & Batist, M. D. (2015). A new methodology for quantifying bubble flow rates in deep water using splitbeam echosounders: Examples from the Arctic offshore NW-Svalbard. *Limnology and Oceanography: Methods*, *13*(6), 267–287. <https://doi.org/10.1002/lom3.10024>
- Wang, C.-C. (2016). *Geological Investigation of Mineral Resource Potential in the Offshore Northeastern Taiwan: Video surveys and sampling of seafloor mineral deposits (1/4)* (Vol. 105–14-B, p. 70). Report of Central Geological Survey. Retrieved from <https://www.grb.gov.tw/search/planDetail?id=11768395>
- Wenau, S., Spiess, V., Keil, H., & Fei, T. (2018). Localization and characterization of a gas bubble stream at a Congo deep water seep site using a 3D gridding approach on single-beam echosounder data. *Marine and Petroleum Geology*, *97*, 612–623. <https://doi.org/10.1016/j.marpetgeo.2018.07.016>
- Westbrook, G. K., Thatcher, K. E., Rohling, E. J., Piotrowski, A. M., Pälike, H., Osborne, A. H., et al. (2009). Escape of methane gas from the seabed along the West Spitsbergen continental margin. *Geophysical Research Letters*, *36*(15). <https://doi.org/10.1029/2009gl039191>
- Woo, G. (1996). Kernel estimation methods for seismic hazard area source modeling. *Bulletin of the Seismological Society of America*, *86*(2), 353–362. <https://doi.org/10.1785/BSSA0860020353>